www.czasopisma.pan.pl PAN POLSKA AKADEMIA NAUK www.journals.pan.pl

Arch. Metall. Mater. **66** (2021), 1, 267-272

DOI: 10.24425/amm.2021.134784

H. AGHABEYGZADEH[1], E. MOHAMMAD SHARIFI[1*], M. TAVOOSI[1]

CORROSION BEHAVIOR OF AMORPHOUS-NANOCRYSTALLINE $Ni_{50}Ti_{50}$ SHAPE MEMORY ALLOY

In the present study, the corrosion behaviors of amorphous-nanocrystalline $Ni_{50}Ti_{50}$ shape memory alloy with different crystallite sizes were investigated. The $Ni_{50}Ti_{50}$ homogenized specimens were hot rolled and annealed at 950°C. Thereafter, the nanocrystalline $Ni_{50}Ti_{50}$ specimens with different crystalline sizes in the range of 40-350 nm were prepared by cold rolling and annealing at temperature range of 400 to 900°C. The corrosion resistance of $Ni_{50}Ti_{50}$ specimen with coarse grain size has significantly increased after cold rolling as a result of the formation of amorphous-nanocrystalline structure. The amorphous and nanocrystalline (with the crystallite size of about 40 nm) $Ni_{50}Ti_{50}$ samples exhibited the best corrosion resistance in the 5% HCl electrolyte with the corrosion potential and corrosion current density of about –197 mV and 2.34×10^{-6} A/cm^2, respectively. This effect can be attributed to the higher density of crystalline defects in amorphous and nanocrystalline structures to quickly form protective films on the surface.

Keywords: NiTi, Shape memory alloy, Amorphous, Nanocrystalline, Corrosion

1. Introduction

Nanocrystalline materials, a class of materials with crystalline size smaller than 100 nm, are characterized by their high volume fraction of grain boundary as much as 10-50% of the total crystal volume [1-3]. The small grain size and the high volume fraction of grain boundaries in these materials may exhibit different corrosion behaviors from that of coarse grain counterparts. Based on theoretical aspects, nanocrystalline materials with high volume fraction of structural defects as active corrosion locations are prone to corrosion [4]. More recent studies about corrosion properties of these materials pointed out that, in some cases, the corrosion resistance can improve with reducing the grain size to nano scale. The solute dilution effect by grain size refinement [5], texture changes with decreasing grain size and grain size-dependent of passive layer formation are important explanations proposed for this effect. However, good understanding of the relation between the corrosion properties and microstructure of nanocrystalline materials is important for both prospective engineering applications and knowledge of fundamental physicochemical properties [5,6].

$Ni_{50}Ti_{50}$ shape memory alloy (SMA) exhibits excellent superelastic and shape memory behavior, high corrosion resistance and biocompatibility [7,8]. This alloy is generally regarded as highly corrosion resistant. This is because of the formation of a passive titanium oxide layer on the surface of the alloy. Even a weak oxidizing environment in contact with NiTi at low temperature is sufficient to produce a few nanometers of a stable TiO_2 film. Based on highly corrosion resistance and biocompatibility, this alloy is commercially used in orthopedic implants and medical devices such as dental wires, bone fraction fixation plate and staples, and etc. [9-11].

The functional properties of SMA such as the recovery strain, shape recovery rate, recovery stress, temperature range of shape recovery and transformation yield stress, are structure-sensitive ones. Therefore, various thermomechanical treatments like cold rolling and subsequent annealing causing a well-developed dislocation substructure or nanocrystalline structure are effectively used for improving the superelastic properties of SMAs [12]. Nanocrystalline shape memory alloys have superior properties over their coarse grained counterparts. Prokofive et al. [13] reported that the formation of nanocrystalline structure in NiTi led to a higher strength of the alloy, with the effect on superelasticity, narrow hysteresis and low residual strain.

Although many efforts have been done through the formation and characterizations of amorphous-nanocrystalline $Ni_{50}Ti_{50}$ phase [14,15], there are few reports regarding the effect of microstructure on the corrosion behavior of this material. Thus, the goal of this work is to investigate the corrosion behaviors of amorphous-nanocrystalline $Ni_{50}Ti_{50}$ shape memory alloys with

[1] MALEK ASHTAR UNIVERSITY OF TECHNOLOGY, DEPARTMENT OF MATERIALS ENGINEERING, P.O. BOX 83145/115, SHAHIN SHAHR, ISFAHAN, IRAN

* Corresponding author: ehsan_sharifi_2000@yahoo.com

different structure and crystallite sizes. Moreover, the effects of rolling and annealing processes on corrosion properties of this alloy were analyzed.

2. Experimental procedure

The $Ni_{50}Ti_{50}$ ingot was prepared by melting of the constituent elements (Ni and Ti plates with purity higher than 99.8 wt. %) by a copper boat vacuum induction melting (with the working frequency and the nominal power of 330 kHz and 45 kW, respectively). The as-cast ingot was homogenized at 900°C for 4 h in a vacuum furnace followed by cold water quenching. After homogenization, the specimens were hot rolled at 950°C in to a sheet of 2.5 mm thickness and then annealed at 900°C for 1 h followed by water quenching. The annealed specimens were cold rolled up to 70% thickness reduction at room temperature. Annealing of the samples was performed at temperature range of 400 to 900°C for 1 h followed by water quenching. Before annealing, the specimens were sealed in a quartz ampoule under the vacuum of 10^{-3} Pa.

The microstructure evolutions of the $Ti_{50}Ni_{50}$ alloy were investigated by means of X-ray diffraction (XRD), differential scanning calorimetry (DSC), scanning electron microscopy (SEM) and transmission electron microscopy (TEM) techniques. A Philips X-PERT MPD diffractometer was used for XRD measurements using filtered Cu Kα radiation (λ = 0.1542 nm). The XRD patterns were recorded in the 2θ range of 20-80° with the step size of 0.03° and time per step of 1 s). Scherrer method [16] was used to evaluate the crystallite size of $Ni_{50}Ti_{50}$ phase. DSC measurement (DSCNETZSCH200F3) was performed with a heating rate of 10°C/min. The structural characterizations of samples were studied using a field emission scanning (VEGA-TESCAN-XMU) and transmission (TEMJEOL-2100F) electron microscopy. Samples for TEM investigations were prepared by polishing with a twin-jet electro-polisher (Struers, Tenupol-5) in a solution of 90% acetic acid glacial and 10% perchloric acid at 15°C under 35 V. TEM observations were made at the operating voltage of 200 kV. The corrosion behaviors of prepared samples were examined by polarization corrosion testing method using a potentiostat system (EG&G Model 273A). All corrosion tests were performed in 5% HCl electrolyte with the reference electrode of Ag/AgCl. A platinum foil was used as counter electrode and potentials were controlled with respect to a saturated calomel electrode (SCE). Polarization curves were produced at scan rate of 1 mV/s from –750 mV and +250 mV. Open circuit potential (OCP) measurements were performed at step potential of 0.1 V/s for 3 h.

3. Results and discussion

The XRD patterns of as-homogenized and 70% cold rolled $Ni_{50}Ti_{50}$ samples are presented in Fig. 1. According to this figure, NiTi phase with austenite (B2) structure is the most prominent phase in as-homogenized $Ni_{50}Ti_{50}$ ingot. There are several additional diffraction peaks in this XRD pattern, suggesting the formation of NiTi phase with martensite (B19') structure during casting and homogenizing process. Based on SEM micrographs (Fig. 2), the grain size of austenite phase in as-homogenized sample was estimated of about 50 μm.

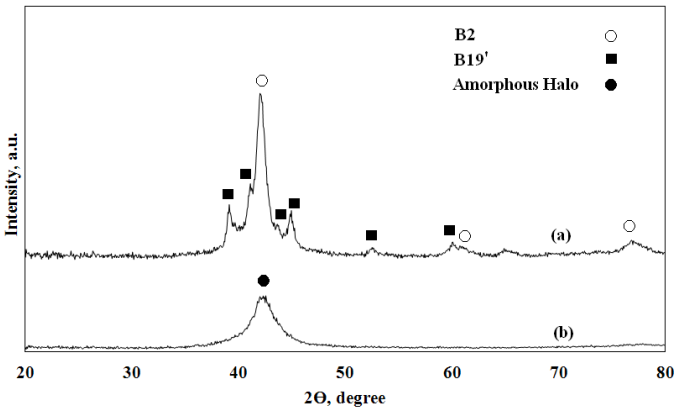

Fig. 1. XRD patterns of a) as-homogenized and b) 70% cold-rolled $Ni_{50}Ti_{50}$ samples

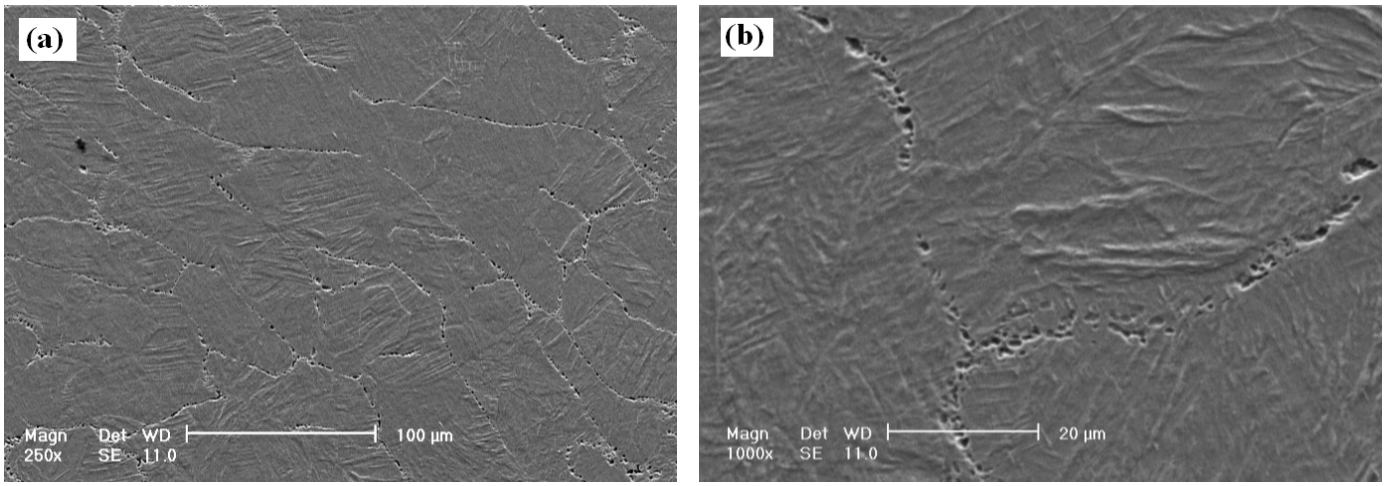

Fig. 2. SEM micrographs of as-homogenized $Ni_{50}Ti_{50}$ sample in two magnifications a) complex overview; b) more detailed view

In order to investigate the structural changes which occur in $Ni_{50}Ti_{50}$ ingot during rolling process, the XRD pattern of 70% cold-rolled sample is presented in Fig. 1(b). As seen, the XRD pattern exhibits one broad diffuse scattering halo (in 2θ range of 40-50°). This could be due to the enhancement of dislocation density during severe plastic deformation and the formation of nanocrystalline or amorphous phases. However, the TEM results and selected area diffraction patterns (SADPs) show that this sample are not completely amorphous and its microstructure is composed of amorphous (A region in Fig. 3) and partially nanocrystalline (B region in Fig. 3) phases. Many studies were carried out to create such a composite structure, which was, nanograins with an amorphous matrix [17-19]. The amorphization mechanism of $Ni_{50}Ti_{50}$ alloy during cold-rolling process could be related to the dislocation accumulation during the deformation process. Twin boundary movement and dislocation slip are the most important deformation modes in martensitic phase of NiTi. The twin boundaries will act as the barriers for the motion of dislocations during deformation and promote their high density accumulation. Thus, dislocation accumulation appears to be a major component of amorphization induced by cold rolling [9].

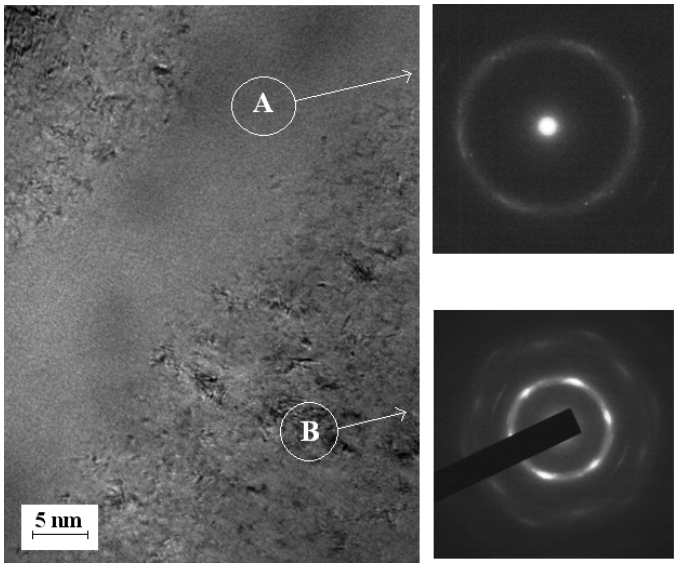

Fig. 3. TEM micrograph and SAD patterns of the 70% cold-rolled $Ni_{50}Ti_{50}$ sample

The polarization curves of as-homogenized and 70% cold-rolled $Ni_{50}Ti_{50}$ samples are presented in Fig. 4. These curves have qualitatively similar behavior but with different values of their electrochemical parameters. Based on polarization curves, during cold-rolling process, the corrosion behavior of $Ni_{50}Ti_{50}$ sample has been changed and the corrosion polarization curves shift to the top left (noble area) of the chart. The corrosion potential and current density of as-homogenized sample are about –250 mV and 5.27×10^{-6} A/cm^2, respectively. It can be observed that after 70% of cold-rolling, the corrosion potential shifts from −250 mV to about −197 mV. In this condition, the corrosion current density decreases evidently from 5.27×10^{-6} to 2.34×10^{-6} A/cm^2. By considering all above features, it can be concluded that the amorphous-nanocrystalline structure exhibits better corrosion resistance in 5% HCl solution compared to the coarse grains counterpart.

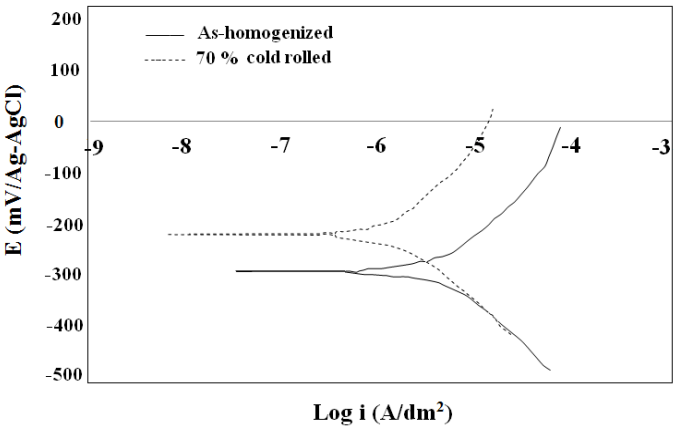

Fig. 4. Polarization Tafel curves of as-homogenized and 70% cold-rolled $Ni_{50}Ti_{50}$ samples in 5% HCl electrolyte

Good corrosion resistance of $Ni_{50}Ti_{50}$ alloy is due to formation of titanium dioxide on the surface of alloy similar to that found in other Ti alloys. TiO_2 has low free energy formation in comparison with TiO and NiO [14,15], thus titanium dioxide forms thermodynamically on the surface of this alloy. The formation kinetic, uniformity and the stability of TiO_2 passive film on the surface has direct effects on corrosion behaviors of $Ni_{50}Ti_{50}$ alloy. Heat treatment, surface composition, surface finishing and the microstructural characteristics are important factors that influence on the stability of the passive film as well as the corrosion properties on this alloy [15]. The enhanced corrosion resistance of $Ni_{50}Ti_{50}$ during cold rolling process can be attributed to the formation amorphous phase in this alloy. The higher corrosion resistance of amorphous alloys can be attributed to:

– The lack of structural defects, such as grain boundaries and second phase particles in these materials. Corrosion processing often occurs preferentially at such sites and therefore amorphous materials might be expected to exhibit corrosion behavior than crystalline materials. The galvanic corrosion, associated with chemical inhomogeneity, is also impossible in these materials.
– The formation of a uniform and protective passive layer on surface. The active dissolution of amorphous materials promotes the accumulation of passivizing species at the alloy-solution interface prior to the formation of the passive film. Moreover, due to the small grain size and high volume fraction of amorphous phase, the diffusion of elements in these materials is much higher than conventional structures. Fast diffusion of Ti atoms in amorphous-nanocrystalline materials, which have a high density of nucleation sites for passive layer, leads to higher fraction of passive layers and lower corrosion rates [20,21]. This phenomenon leads to the formation of a uniform and highly protective passive film on surface [11].

– Increasing the adhesion strength between the passive film and substrate with formation of amorphous- nanocrystalline structures. This phenomenon can be related to the enhancement in the electron activity at non-crystalline regions (amorphous phase as well as grain boundaries) and possible pegging of the passive layer into substrate [22].
– A stable interfacial structure and chemistry could also favorable for corrosion properties [23].

The amorphous phase is a metastable state and considerable structural and phase changes could be occur during heating. In order to study the thermal stability of the prepared amorphous phases, the cold-rolled sample was examined using DSC technique under continuous heating condition. The DSC heating trace of cold-rolled $Ni_{50}Ti_{50}$ sample is presented in Fig. 5. As seen, only one exothermic peak (around 365°C) appears in this DSC curve. To analyze the crystallization process responsible for this exothermic peak, annealing treatment was made at 400°C for 1 h in vacuum. The XRD pattern of the cold-rolled $Ni_{50}Ti_{50}$ sample after annealing process is shown in Fig. 6. As seen, this sample is mainly composed of the NiTi peaks with austenite (B2) structure. There are several narrow diffraction peaks in this XRD pattern, suggesting the formation of NiTi phase with martensitic (B19') structure. Therefore, the exothermic peak in Fig. 5 should be attributed to the formation of the crystalline NiTi phase from the amorphous matrix [24-25]. Annealing of the severely cold-rolled $Ni_{50}Ti_{50}$ alloy activates two competing mechanisms: growth of the deformation-induced grains and crystallization of the amorphous phase, which lead to the formation of nonacrystalline structure. The TEM bright-field images and SADP of this sample are presented in Fig. 7. Essentially nanocrystalline structure (as verified by its continuous diffraction rings) with average crystallite size of about 40 nm is clearly observed in these micrographs. The regions with dark contrast correspond to the nanograins of martensite phase with a relatively larger size. The SADP do not contain diffuse rings corresponding to the amorphous phase, showing the completion of crystallization. The SADP is dominantly indexed to austenite and a few martensite needles. These results are in agreement with the XRD pattern of this sample which is presented in Fig. 6.

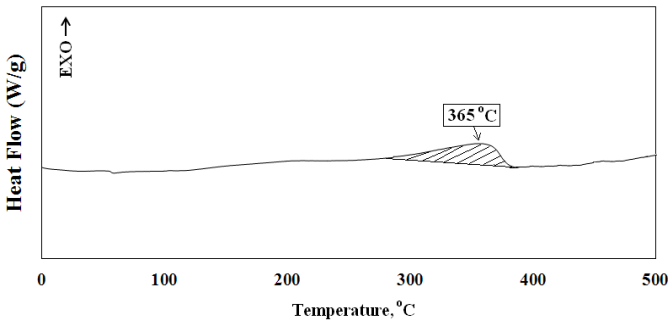

Fig. 5. DSC heating trace of the 70% cold-rolled $Ni_{50}Ti_{50}$ sample

The polarization curves of the 70% cold-rolled sample before and after annealing process at 400°C for 1 h in 5% HCl

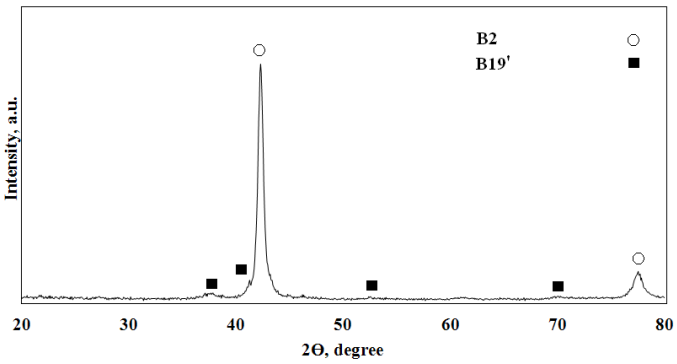

Fig. 6. XRD pattern of the 70% cold-rolled $Ni_{50}Ti_{50}$ sample after annealing at 400°C for 1 h

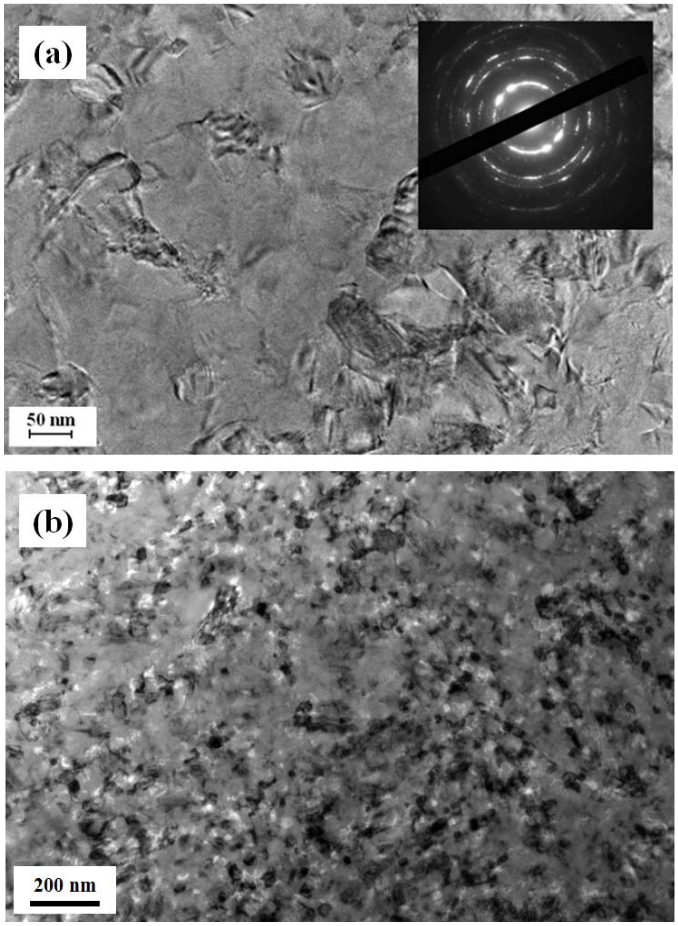

Fig. 7. TEM micrographs and SAD pattern of the 70% cold-rolled $Ni_{50}Ti_{50}$ sample after annealing at 400°C for 1 h

electrolyte are presented in Fig. 8. As seen, there is no significant difference between the polarization curves of cold-rolled (with amorphous structure) and annealed (with nanocrystalline structure) samples. This point illustrates that, corrosion behavior of amorphous and nanocrystalline $Ni_{50}Ti_{50}$ samples are the same. The similar corrosion properties of amorphous and nanocrystalline $Ni_{50}Ti_{50}$ alloy can be attributed to the similar characteristics of passive TiO_2 layer in $Ni_{50}Ti_{50}$ surface.

To investigate the structural changes which occur in nanocrystalline $Ni_{50}Ti_{50}$ sample during annealing, the sample with

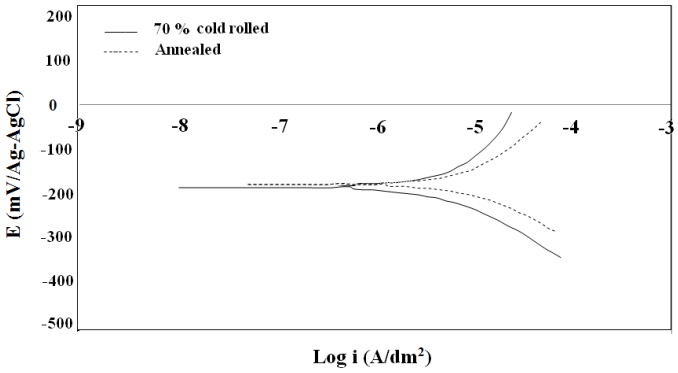

Fig. 8. Tafel polarization curves of 70% cold-rolled $Ni_{50}Ti_{50}$ samples before and after annealing process at 400°C for 1 h in 5% HCl electrolyte

average crystallite size of 40 nm was annealed at 700, 800 and 900°C for 1 h and the annealed samples were examined using XRD technique. Based on the presented XRD patterns in Fig. 9, during annealing process, only a narrowing of the $Ni_{50}Ti_{50}$ peaks with remarkable increase in their intensities have been occurred. In this regards, the crystalline sizes of the $Ni_{50}Ti_{50}$ sample were estimated using Scherrer equation and the results are presented in Table 1. As seen, by increasing the annealing temperature, the crystallite size of nanocrystalline $Ni_{50}Ti_{50}$ sample increases progressively, and reach to the value of about 350 nm in annealed sample at 900°C.

The polarization curves of $Ni_{50}Ti_{50}$ sample before and after annealing at 700, 800 and 900°C are shown in Fig. 10. The corrosion potential and current density of these samples are also presented in Table 1. According to these results, increasing the crystallite sizes during annealing led to changes in the corrosion behaviors of $Ni_{50}Ti_{50}$ alloy. In this condition, the polarization curves shifts to right down sides (active area) of the chart. By considering all above features, it can be concluded that the nanorystalline $Ni_{50}Ti_{50}$ with the larger crystalline size should exhibit poor corrosion resistance in comparison with amorphous-nanocrystalline structure. This point can be related to the more stability and uniformity of formed TiO_2 passive film on amorphous and nanocrystalline $Ni_{50}Ti_{50}$ surface as compared to coarse grains counterparts [22].

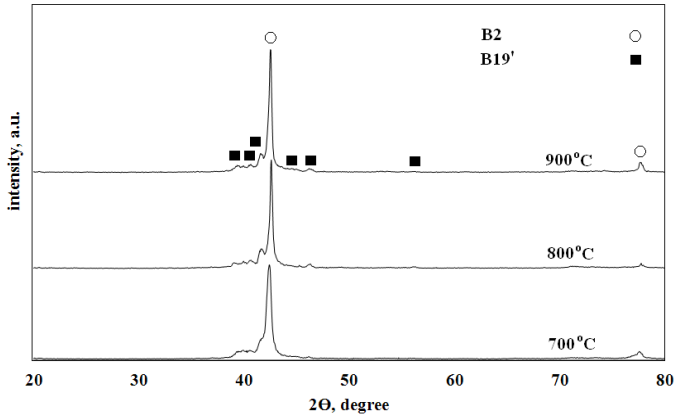

Fig. 9. XRD patterns of the nanocrystalline $Ni_{50}Ti_{50}$ samples after annealing at 700, 800 and 900°C for 1 h

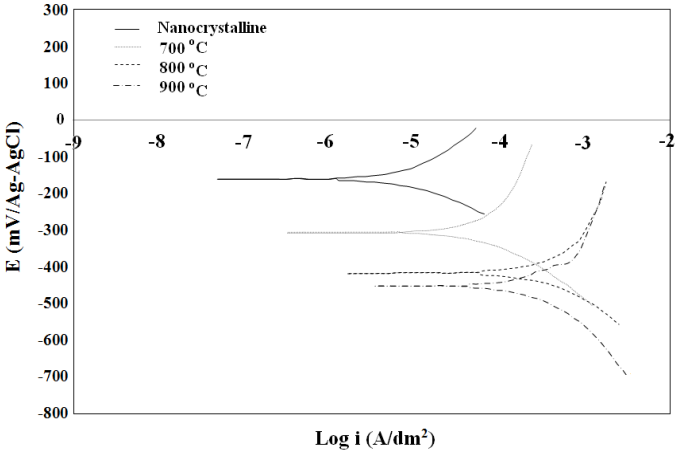

Fig.10. Polarization Tafel curves of nanocrystalline $Ni_{50}Ti_{50}$ samples before and after annealing process at 700, 800 and 900°C for 1 h in 5% HCl electrolyte

TABLE 1

The crystallite sizes, corrosion potential and current density of nanocrystalline $Ni_{50}Ti_{50}$ samples after annealing at different temperature

Temperature, °C	Crystallite size, nm	Corrosion	
		Potential, mV	Current density, A/cm²
700	80	–300	21.24×10^{-6}
800	210	–415	93.4×10^{-6}
900	350	–450	138.6×10^{-6}

4. Conclusions

In the present study, the corrosion behaviors of amorphous-nanocrystalline $Ni_{50}Ti_{50}$ shape memory alloys with different crystallite sizes were investigated. The results indicated that, the corrosion resistance of $Ni_{50}Ti_{50}$ ingot with coarse grain size has significantly increased during cold-rolling process and the formation of amorphous-nanocrystalline structure. The amorphous and nanocrystalline $Ni_{50}Ti_{50}$ samples exhibited the best corrosion resistance as result of the higher density of crystalline defects in amorphous and nanocrystalline structures to quickly form a protective and stable passive film on surface. In this condition, the corrosion potential and current density was estimated about –197 mV and 2.34×10^{-6} A/cm^2, respectively. By annealing, the grain size of nanocrystalline $Ni_{50}Ti_{50}$ sample was increased to about 350 nm and the corrosion potential and current density reached about –450 mV and 138.6×10^{-6} A/cm^2, respectively.

REFERENCES

[1] C. Suryanarayana, Prog. Mater. Sci. **46**, 1-184 (2001).
[2] K.S. Kumar, H. Swygenhoven, S. Suresh, Acta Mater. **51**, 5743-5774 (2003).
[3] H.S. Kim, M.B. Bush, Nanostruct. Mater. **11**, -367 (1999).

[4] K.D. Ralston, D. Fabijanic, N. Birbilis, Electrochim. Acta **56**, 1729-1736 (2011).
[5] K.T. Liu, J.G. Duh, J. Electronal. Chem. **618**, 45-52 (2008).
[6] G.R. Argade, S.K. Panigrahi, R.S. Mishra, Corros. Sci. **58**, 145-151 (2012).
[7] D.C. Lagoudas (Ed.), Shape Memory Alloys: Modeling and Engineering Applications, Springer, Texas (2008).
[8] K. Otsuka, C.M. Wayman, Shape Memory Materials, Cambridge University Press, Cambridge (1998).
[9] K. Otsuka, X. Ren, Prog. Mater. Sci. **50**, 511-678 (2005).
[10] K. Otsuka, X. Ren, Intermetallics **7**, 511-528 (1999).
[11] S. Civjan, E.F. Huget, L.B. DeSimon, J. Dent. Res. **54**, 89-96 (1975).
[12] E. Mohammad sharifi, A. Kermanpur, T. Nonferr. Metal. Soc. **28**, 515-523 (2018).
[13] E. Prokofiev, J. Burow, J. Frenzel, D. Gunderov, G. Eggeler, R. Valiev, Mater. Sci. Forum **667-669**, 1059-1064 (2011).
[14] J. Khalil-Allafi, B. Amin-Ahmadi, M. Zare, Mat. Sci. Eng. C **30**, 1112-1117 (2010).
[15] T. Duerig, A. Pelton, D. Stöckel, Mat. Sci. Eng. A **273**, 149-160 (1999).
[16] R.D. Barrett, S.E. Bishara, J.K. Quinn, Am. J. Orthod. Dentofac. **103**, 8-14 (1993).
[17] H. Li, L. Lou, F. Hou, D. Guo, W. Li, X. Li, D. Gunderov, K. Sato, X. Zhang, Appl. Phys. Lett. **103**, 142406 (2013).
[18] X. Li, L. Lou, W. Song, G. Huang, F. Hou, Q. Zhang, H. Zhang, J. Xiao, B. Wen, X. Zhang, Adv. Mater. **29**, 1606430 (2017).
[19] X. Li, L. Lou, W. Song, Q. Zhang, G. Huang, Y. Hua, H. Zhang, J. Xiao, B. Wen, X. Zhang, Nano Lett. **17**, 2985-2993 (2017).
[20] B. Basak, A.K. Sengupta, Scripta Mater. **51**, 225-229 (2004).
[21] K.M.S. Youssef, C.C. Koch, P.S. Fedkiw, Corros. Sci. **46**, 51-64 (2004).
[22] L. Wang, Y. Lin, Z. Zeng, W. Liu, Q. Xue, L. Hu, J. Zhang, Electrochim. Acta **52**, 4342-4350 (2007).
[23] G. Huang, X. Li, L. Lou, Y. Hua, G. Zhu, M. Li, H. Zhang, J. Xiao, B. Wen, M. Yue, X. Zhang, Small **14**, 1800619 (2018).
[24] S.D. Prokoshkin,V. Brailovski, K.E. Inaekyan,V. Demers, I. Khmelevskaya, S.V. Dobatkin, E. Tatyanin, Mat. Sci. Eng. A **481-482**, 114-118 (2008).
[25] K. Tsuchiya, M. Inuzuka, D .Tomus, A. Hosokawa, H. Nakayama, K. Morii, Y. Todaka, M. Umemoto, Mat. Sci. Eng. A **438-440**, (2006) 643-648.